



Scaling of relaxation and excess entropy in plastically deformed amorphous solids

K. Lawrence Galloway^{a,1}, Xiaoguang Ma^{b,c,1,2}, Nathan C. Keim^d, Douglas J. Jerolmack^{a,e}, Arjun G. Yodh^b, and Paulo E. Arratia^a

^aDepartment of Mechanical Engineering and Applied Mechanics, University of Pennsylvania, Philadelphia, PA 19104; ^bDepartment of Physics and Astronomy, University of Pennsylvania, Philadelphia, PA 19104; ^cComplex Assemblies of Soft Matter, CNRS–Solvay–UPenn UMI 3254, Bristol, PA 19007–3624; ^dDepartment of Physics, Pennsylvania State University, University Park, PA 16802–6300; and ^eDepartment of Earth and Environmental Science, University of Pennsylvania, Philadelphia, PA 19104

Edited by David A. Weitz, Harvard University, Cambridge, MA, and approved April 9, 2020 (received for review January 13, 2020)

When stressed sufficiently, solid materials yield and deform plastically via reorganization of microscopic constituents. Indeed, it is possible to alter the microstructure of materials by judicious application of stress, an empirical process utilized in practice to enhance the mechanical properties of metals. Understanding the interdependence of plastic flow and microscopic structure in these nonequilibrium states, however, remains a major challenge. Here, we experimentally investigate this relationship, between the relaxation dynamics and microscopic structure of disordered colloidal solids during plastic deformation. We apply oscillatory shear to solid colloidal monolayers and study their particle trajectories as a function of shear rate in the plastic regime. Under these circumstances, the strain rate, the relaxation rate associated with plastic flow, and the sample microscopic structure oscillate together, but with different phases. Interestingly, the experiments reveal that the relaxation rate associated with plastic flow at time t is correlated with the strain rate and sample microscopic structure measured at earlier and later times, respectively. The relaxation rate, in this nonstationary condition, exhibits power-law, shear-thinning behavior and scales exponentially with sample excess entropy. Thus, measurement of sample static structure (excess entropy) provides insight about both strain rate and constituent rearrangement dynamics in the sample at earlier times.

amorphous solids | plasticity | shear | relaxation | excess entropy

For many amorphous solids—i.e., solids without long-range order—a threshold stress exists beyond which the material starts to deform plastically (yield) and flow like a liquid. These yield stress materials, which range from foams and colloids to cement and metallic glasses, have constituents and dynamics that vary widely across length and time scales (1–3). Nevertheless, they are unified by two features: the cross-over transition from solid- to liquid-like behavior and a nonlinear viscosity response to external stress (shear thinning) (4). Ultimately, to understand these nonlinear mechanical processes, we need a detailed picture about how shear couples to microscopic structure and relaxation. If successful, this understanding could lead to improved processing of amorphous metals via stress-induced control of microstructure (5, 6).

To this end, useful models have been developed to characterize the structural origin of plasticity in amorphous solids. Shear transformation zone models, for example, posit the existence of mechanically weak regions in amorphous solids analogous to crystalline defects, and then they focus (largely) on the kinetics associated with localized plastic events (7). The softer regions are believed to facilitate or accelerate rearrangements nearby. This general phenomenology of dynamic heterogeneity is observed in experiments (8) and computer simulations (7) and is supported by first-principle Mode-Coupling and Random First-Order Transition theories (9–11). Nevertheless, identification of mechanically weak regions from static sample structure—e.g., before plastic events occur—remains a challenge.

In a different vein, thermodynamic predictors based on excess entropy (S^{ex}) have shown promise for explaining nonlinear mechanical phenomena in complex fluids (12–17). Excess entropy concepts were developed from studies of liquids rather than solids; they facilitate comparison of macroscopic system-averaged structural and dynamical quantities. S^{ex} is a structural order parameter defined as the difference between system thermodynamic entropy and that of an equivalent ideal gas (18). For typical liquids, S^{ex} derives mainly from pair correlations of its constituents (13) and is readily evaluated by experiment (15, 19). Excess entropy accurately predicts transport coefficients of simple and complex fluids in equilibrium using their static structure (15, 19–30). Recently, in computer simulations, S^{ex} has been applied to supercooled liquids under steady-state shear; the shear-dependent relaxation time of the supercooled liquids was found to scale with S^{ex} (16), thereby revealing a simple structural connection to shear-thinning induced relaxation. This intriguing discovery has not been tested experimentally. Moreover, the concept of excess entropy scaling has not been applied to understand plastic flow in amorphous solids, nor in materials driven into more general nonstationary states.

In this contribution, we investigate the connection between shear rate, relaxation time, and excess entropy of plastically

Significance

When stressed sufficiently, many solids plastically deform and flow. This plastic deformation induces irreversible structural changes, which are sometimes used in practice to manipulate microstructure of materials to achieve desired mechanical properties. Unfortunately, our limited fundamental understanding of the interdependence of plastic flow and microstructure represents a design barrier for improvement of strength, hardness, and ductility in amorphous solids, where constituent particles are haphazardly arranged. Here, we study plastic flow and its influence on the microstructure of disordered colloidal solids. Video images, with single-particle resolution, reveal connections between bulk mechanical response and microstructure during plastic deformation. Specifically, structural relaxation induced by plastic flow depends on strain rate at earlier times and predicts microscopic structural features at later times.

Author contributions: X.M. designed research; K.L.G. and X.M. performed research; K.L.G. and N.C.K. performed experiment; K.L.G. and X.M. analyzed data; and K.L.G., X.M., N.C.K., D.J.J., A.G.Y., and P.E.A. wrote the paper.

The authors declare no competing interest.

This article is a PNAS Direct Submission.

Published under the PNAS license.

¹K.L.G. and X.M. contributed equally to this work.

²To whom correspondence may be addressed. Email: xiaom@seas.upenn.edu.

This article contains supporting information online at <https://www.pnas.org/lookup/suppl/doi:10.1073/pnas.2000698117/-DCSupplemental>.

deformed matter in nonstationary states. We use a custom-made interfacial stress rheometer (31–34) to apply oscillatory shear at different strain amplitudes to an oil–water interface (Fig. 1A; see *Materials and Methods* for details). A series of disordered, two-dimensional (2D) colloidal solids were prepared at the oil–water interface (Fig. 1B). Their translational and orientational correlation functions did not exhibit long-range order (*SI Appendix*). The disordered samples were driven by the applied oscillatory shear, and, concurrently, the trajectories of individual particles in the samples were captured by video optical microscopy and standard tracking software.

From particle position data during oscillatory shear, we computed strain rate, the relaxation rate/time associated with plastic flow, and the sample excess entropy. The relaxation time exhibited a power-law scaling with shear rate, a characteristic of shear-thinning behavior. Furthermore, phase shifts between the oscillatory signals revealed a constant lag time between plastic shear rate and plastically induced relaxation rate, and a different lag time between relaxation rate and excess entropy (which was proportional to the instantaneous relaxation time). These delay intervals (phase shifts) uncovered connections between shear rate, plastic flow-induced relaxation, and structure of the samples in nonstationary states. Surprisingly, we found that relaxation time/rate and excess entropy data measured at different strain amplitudes collapsed onto a single master exponential scaling curve which depends only on sample type. In total, the work introduces an analysis framework based on excess entropy scaling to understand plastic flow in both stationary and nonstationary states, and the findings suggest that information about the relaxation history of an amorphous material can be deduced from its current static structure.

Briefly, the solid-like monolayers consist of colloidal spheres with different diameters (σ), surface charge densities, and packing fractions (ϕ) (Table 1 and *Materials and Methods*). In combination, these factors determine interparticle separation (d), sample structure (Fig. 1C and D and *SI Appendix*), shear moduli, and plasticity (33, 34). Rheology measurements of the samples exhibit elastic behavior at small strain amplitudes and yielding behavior when the strain exceeds about 3% (*SI Appendix*). Herein, we focus exclusively on strain amplitudes above the yield point (e.g., larger than 5%; Table 1).

We first used the particle trajectory data to measure and compare shear rates and shear-induced relaxation times. The shear strain, $\Gamma(t)$, at time t quantifies the sample's affine deformation, which follows the oscillations of the needle motion. We computed $\Gamma(t)$ by taking average of the measured y -dependent local strain, $\gamma(y, t)$ (*Materials and Methods*). Fig. 2A shows that $\dot{\Gamma}(t)$

follows the driving sinusoidal function set by the external force and that it exhibits measurable fluctuations about the sinusoidal function too. Note that fluctuations of $\Gamma(t)$ about the driving stress have been seen in plastically deformed bidisperse polycrystals in computer simulations (35, 36); these fluctuations were attributed to intermittent yielding along grain boundaries and become weaker when the sample has smaller crystalline domains.

We used nonaffine particle motions to evaluate sample relaxation behavior (16, 37). At time t , the self-part of the intermediate scattering function is

$$F_s(t, \tau) = \frac{1}{N} \left\langle \sum_{j=1}^N \exp \left[\frac{2\pi i}{d} |\Delta \vec{r}'_j(\tau)| \right] \right\rangle. \quad [1]$$

Here, N is the number of particles and $\Delta \vec{r}'_j$ the nonaffine displacement of the j -th particle—that is, the residual after the affine displacement has been subtracted from the total particle displacement, $\Delta \vec{r}_j$. (See *Materials and Methods* and *SI Appendix* for how to compute $\Delta \vec{r}'_j$ from $\Delta \vec{r}_j$.) The brackets, $\langle \dots \rangle$, represent a time average over the period $[t - \delta t/2, t + \delta t/2]$ ($\delta t = 2.5$ s is one-quarter of the shear cycle). The duration of the measurement is thus δt . Ideally, $F_s(\tau)$ should decay to below $1/e$ at $\tau = \delta t$ to extract the relaxation time. However, we will soon show that this is not necessary.

Fig. 2B shows examples of $F_s(t, \tau)$ at two times where the $\dot{\Gamma}$ values are different; these $F_s(t, \tau)$ functions decay at different rates, indicating shear-dependent relaxation behavior. $F_s(t, \tau)$ is well fit by the function,

$$F_s(t, \tau) = A \exp[-(\tau/\tau_\alpha)^\beta], \quad [2]$$

where τ_α is the α -relaxation time measured in the time interval centered on t , and $A \simeq 1$ is a constant prefactor (*SI Appendix*). Since we can fit $F_s(\tau)$ data before it decays to $1/e$ to obtain τ_α , we can estimate τ_α from measurements with duration (δt) shorter than τ_α (see *SI Appendix* for details). Interestingly, we found $\beta > 1$ (compressed exponential) throughout the shear cycle in all samples. This finding confirms the expectation that particle configurations, when driven by external forces, relax/reorganize faster than would occur if driven by diffusive motions alone. A few studies have also reported $\beta > 1$ phenomena (38–43); in these cases, ballistic motions of constituents were found to accompany the accumulation and release of internal stress (44). In our experiments, the nonaffine mean square displacements, $\langle \Delta r'^2(\tau) \rangle$, exhibit superdiffusive behavior—that is, $\langle \Delta r'^2(\tau) \rangle \sim \tau^p$ with $p > 1$ (*SI Appendix*); by analogy to prior

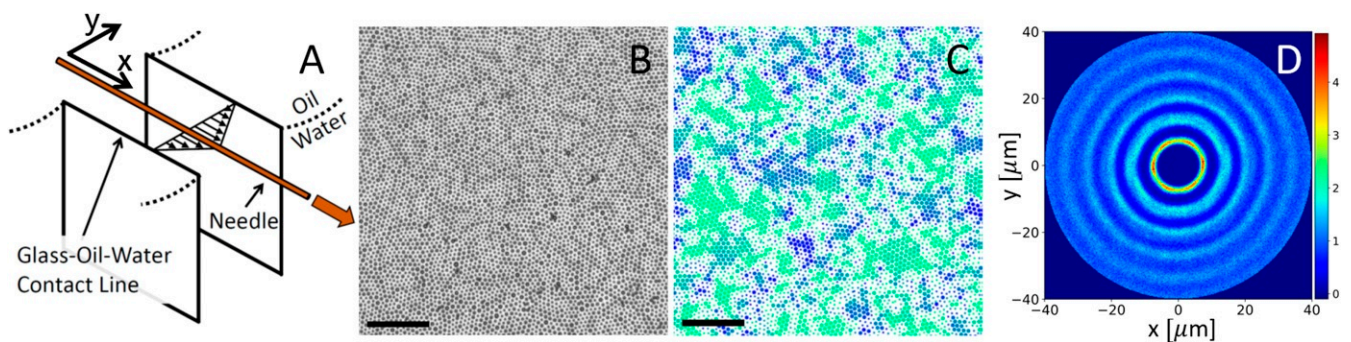


Fig. 1. (A) Schematic of the interfacial stress rheometer. A sinusoidal magnetic force is imparted to the interface-bound magnetic needle, which, in turn, introduces oscillatory shear stress at the oil–water interface. The parallel and perpendicular directions with respect to the needle motion are defined as the x and y axis, respectively. (B) Micrograph of bidisperse colloidal particles at the oil–water interface from sample A. (C) Sixfold bond orientation order, ψ_6 , measured from particles in B. Colors help to indicate the lattice director (orientation) as a guide for the eye to help discern ordered and disordered domains. Dots with large size indicate $|\psi_6| > 0.9$, and small dot size indicates $|\psi_6| < 0.9$. (Scale bars: 100 μm). (D) A pair correlation function, $g(x, y)$, measured from particle positions in B exhibits strong anisotropy due to ordered domains.

Table 1. Different colloidal monolayers

Sample	σ , μm	ϕ , %	d , μm	Γ_{max} , %
A (bidisperse)	4.1, 5.6	43	7.4	5 to 16
B (monodisperse)	5.6	32	7.7	8 to 16
C (bidisperse)	1.0, 1.2	32	9.8	5 to 8

σ , particle diameter; ϕ , packing fraction; d , mean interparticle separation; Γ_{max} , strain amplitude.

work, we believe the measured compressed exponential decay of $F_s(t, \tau)$ is caused by superdiffusive particle motions. We also investigated alternative explanations for the compressed exponential decay of $F_s(\tau)$ (SI Appendix).

Using the $\dot{\Gamma}(t)$ and $\tau_\alpha(t)$ data, we next investigated how shear influences relaxation in the nonstationary regime. Fig. 2C compares $|\dot{\Gamma}(t)|$ and $\tau_\alpha^{-1}(t)$ measured from sample A ($\Gamma_{\text{max}} = 16\%$) as a function of t ; here, the absolute shear rate was used because we expected the shear direction to have little influence on relaxation rate. This comparison clearly demonstrates that the relaxation rate lags the shear rate by a time interval, $\Delta t \simeq 0.8$ s (Materials and Methods and SI Appendix). This lag time hints at a causal relation between shear and the shear-induced relaxation processes. Moreover, the amplitude of $\tau_\alpha^{-1}(t)$ follows $|\dot{\Gamma}(t)|$.

For a more quantitative comparison, we examined our data in the context of the non-Newtonian relationship between shear rate and relaxation time that has been found in steady state (45, 46):

$$\tau_\alpha \sim (1 + \dot{\Gamma}/\dot{\Gamma}_0)^\mu. \quad [3]$$

Here, $\dot{\Gamma}_0$ is the shear rate associated with onset of non-Newtonian viscous response behavior, and $\mu < 0$ is a power-law exponent characterizing shear-thinning behavior.

In oscillatory measurements, Eq. 3 has been established between the mean (or maximal) viscosity and shear rate during multiple shear cycles (47). To our knowledge, this relation has not been used to describe the connection between the

instantaneous viscosity (or relaxation time) and shear rate in nonstationary samples. Despite the phase shift between the shear rate and the shear-induced relaxation rate, we might expect our data to follow Eq. 3 with $\dot{\Gamma}$ being replaced by its weighted time average, $\langle |\dot{\Gamma}| \rangle_{\delta t}$, over the time interval $[t - \delta t/2, t + \delta t/2]$ (that is, the same window wherein $\tau_\alpha(t)$ is evaluated; see Materials and Methods and SI Appendix about calculation of $\langle |\dot{\Gamma}| \rangle_{\delta t}$). To test this hypothesis, we plot $\tau_\alpha(t + \Delta t)$ versus $\langle |\dot{\Gamma}(t) \rangle_{\delta t}$ measured from sample A in Fig. 2D. Remarkably, the data from sample A sheared at three different strain amplitudes collapse onto a single master curve; the best fit using Eq. 3 gives $\dot{\Gamma}_0 = (1.7 \pm 0.5) \times 10^{-3} \text{ s}^{-1}$ and $\mu = -1.4 \pm 0.3$. Interestingly, the fitted $\dot{\Gamma}_0$ in our sample is of the same order of magnitude as the onset shear rates of nonlinear viscous response in molecular glasses (45). The fitted μ is similar to those measured in dense suspensions of soft colloidal particles (48). This finding suggests an interesting way to characterize shear-thinning behavior in a nonstationary (e.g., oscillatory) measurement. Note, while in principle the lag time, Δt , between shear rate and relaxation time may be a complex function of shear rate, in our samples it suffices to use a constant lag time.

Next, we computed excess entropy from particle positions and explored whether excess entropy scaling laws can be applied in systems experiencing nonstationary (oscillatory) shear. If the scaling relation still holds, then, by implication, sample static structure can provide information about relaxation induced by plastic deformation. Previously, viscosity, diffusion coefficients, and relaxation times have been found to obey a simple excess entropy scaling law, $\tau_\alpha \sim f(S^{ex})$, for a wide variety of materials (20–30) spanning different particle type, size, density, interaction, temperature, material phase, and even shear rate (16, 24). Importantly, S^{ex} is well approximated by the two-body contribution, S_2 , which is readily determined from scattering or imaging experiments (15, 19, 27).

To this end, we computed the time-dependent pair correlation function, $g(r)$, using particle positions at time t . Note that

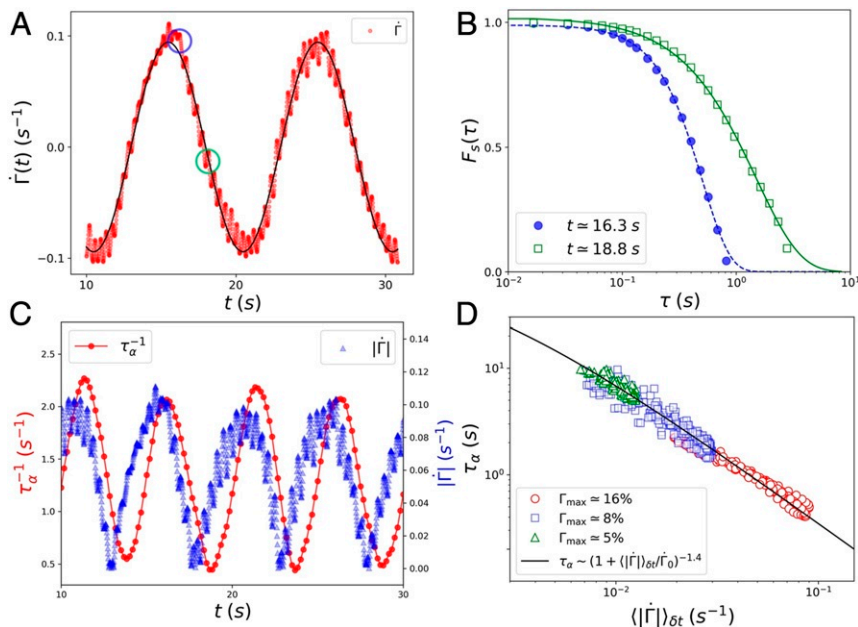


Fig. 2. Dynamics in sample A. (A) Instantaneous shear rate, $\dot{\Gamma}(t)$ versus time, t . The solid line is the sinusoidal fit, $\dot{\Gamma}(t) = 0.096\sin(\omega t)$. (B) The self-part of the intermediate scattering function, $F_s(\tau)$, measured at the two times indicated by the same-color circles (green and blue) as in A. The dashed and solid lines are fits using Eq. 2, with $\tau_\alpha = 0.5$ and 2.3 s and $\beta = 1.3$ and 1.5 at $t = 16.3$ and 18.8 s, respectively. (C) Relaxation rate, $\tau_\alpha^{-1}(t)$, versus time, t (red circles). The magnitude of shear rate, $|\dot{\Gamma}(t)|$, is also plotted (blue triangles) for phase-shift comparison. (D) The measured relaxation time, $\tau_\alpha(t + \Delta t)$, versus time-averaged shear rate, $\langle |\dot{\Gamma}(t) \rangle_{\delta t}$, from three experiments with different Γ_{max} values. The solid line is the best fit using $\tau_\alpha \sim (1 + \langle |\dot{\Gamma}| \rangle_{\delta t} / 0.0017)^{-1.4}$.

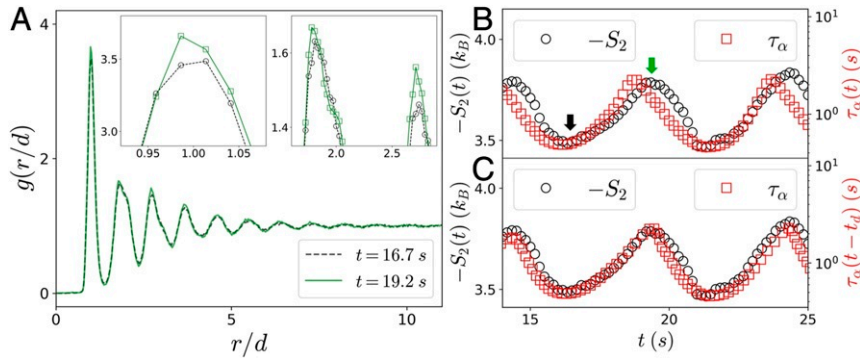


Fig. 3. (A) Measured $g(r)$ from data taken at $t = 16.7$ and 19.2 s. *A*, *Insets* show the enlarged plots of the first (*Left Inset*) and the second and third peaks (*Right Inset*) of $g(r)$, respectively. (B) $S_2(t)$ versus t . $\tau_\alpha(t)$ is also plotted for comparison. The black and green arrows indicate $t = 16.7$ and 19.2 s, respectively. (C) $\tau_\alpha(t - t_d)$ is plotted with a time delay, $t_d(t) \simeq 0.3\tau_\alpha(t)$.

we employed particle coordinates in a single video frame at time t for determination of $g(r)$; these particles were the same as used above in computing $\dot{\Gamma}(t)$ and $\tau_\alpha(t)$. Examples of $g(r)$ at two times, $t = 16.7$ and 19.2 s, are shown in Fig. 3A. These $g(r)$ functions exhibit quasi-long-range order extending out to 10 shells of neighbors; the extended correlations are indicative of the presence of many small crystalline domains (Fig. 1C and *SI Appendix*). By comparison, $g(r)$ from sheared glass-forming liquids typically exhibits only three well-defined peaks (e.g., refs. 16 and 37). The correlation lengths obtained from the spatial correlations of translational and orientational order also confirmed that the samples were more ordered than traditional glasses, but less ordered than crystals/polycrystals (*SI Appendix*).

The peaks of $g(r)$ evolved subtly throughout imposed shear cycles (Fig. 3A, *Insets*); these changes are indicative of shear-induced restructuring. The comparatively high peaks in $g(r)$ at $t = 19.2$ s compared to $t = 16.7$ s suggest a more ordered structure in the former case. The differences in peak height at different times were rather small and were in accord with measurements in sheared molecular glasses (14, 16, 37). From the time-dependent $g(r)$ data, we computed S_2 versus t ,

$$S_2 = -\pi\rho \int_0^\infty \{g(r)\ln[g(r)] - [g(r) - 1]\}rdr. \quad [4]$$

Here, ρ is sample particle number density. Eq. 4 converges quickly after r reaches $5d$ (*SI Appendix*); thus, we chose the cutoff length, $r_{\text{cut}} = 10d$, as the integration limit for computing S_2 . We confirmed that with the same cutoff length, Eq. 4 converges for the other two samples as well (*SI Appendix*). A larger $-S_2$ value at $t = 19.2$ s confirms a more ordered structure, consistent with $g(r)$ data in Fig. 3A. Note that larger $-S_2$ values are also accompanied by larger bond orientation order (49), suggesting that the orientational order is coupled to translational order by shear (*SI Appendix*).

Fig. 3B presents $S_2(t)$ and $\tau_\alpha(t)$ as a function of t during the shear cycles. Notice that longer relaxation times, τ_α , are accompanied by larger $-S_2$ values or, equivalently, more ordered sample structures. Taken together with the $\dot{\Gamma}(t)$ findings (Fig. 2C), we conclude that faster shear rates lead to shorter shear-induced relaxation times and more disordered resultant particle arrangements.

Further inspection of Fig. 3B reveals that the peaks of $-S_2(t)$ clearly lag behind those in $\tau_\alpha(t)$; by comparison, the lags between valleys are less apparent. A possible explanation is that $S_2(t)$ lags behind $\tau_\alpha(t)$ at all phase positions; this hypothesis is further supported by the hysteresis loops generated by the two functions (*SI Appendix*). Based on this intriguing obser-

vation, we hypothesize that 1) the relaxation time measured at t is related to the sample structure (S_2) at a later time, $t + t_d$; and 2) the time delay, $t_d(t)$, is a function of $\tau_\alpha(t)$. We assume $t_d(t) \simeq h\tau_\alpha(t)$, where h is a constant throughout the shear cycles. To test this hypothesis, we replotted $\tau_\alpha(t - t_d)$ in Fig. 3C. The relation $t_d(t) \simeq 0.3\tau_\alpha(t)$ best aligns the peaks and the valleys of $\tau_\alpha(t - t_d)$ and $-S_2(t)$ (*Materials and Methods* and *SI Appendix*). Note that the choice of a linear function of τ_α to approximate t_d is empirical; t_d could have a more complex dependence on τ_α , $\dot{\Gamma}$, and their time derivatives. This empirical finding that $t_d \sim \tau_\alpha$ suggests a picture wherein new structures driven by shear-induced relaxation evolve to their final form after a waiting time that is itself dependent on the relaxation process/timescale. Moreover, the introduction of this form for t_d enables comparison of τ_α versus S_2 across different times and conditions.

To this end, we investigated the scaling connection between τ_α and S_2 obtained at the different shear rates. Fig. 4 shows $\tau_\alpha(t - t_d)$ as a function of $S_2(t)$ for all three samples listed in Table 1. For sample A, data from three strain amplitudes, $\Gamma_{\text{max}} = 16$, 8, and 5%, collapse onto a single master curve. Therefore, we confirm that $\tau_\alpha(t - t_d)$ is a simple monotonic function of $S_2(t)$ in nonstationary oscillatory conditions. Moreover, the

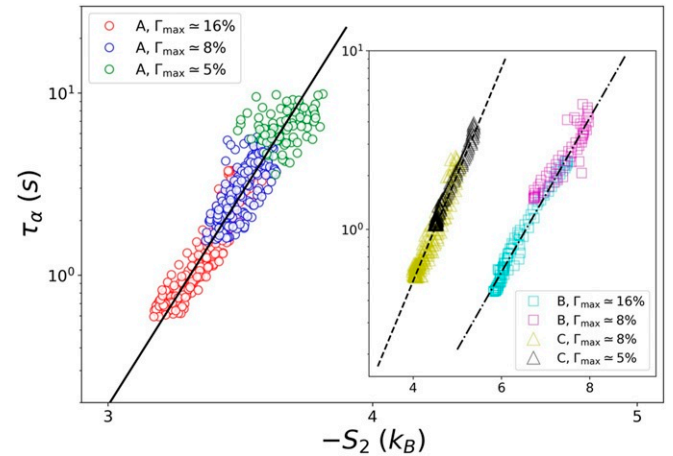


Fig. 4. Delayed relaxation time, $\tau_\alpha(t - t_d)$, as a function of the excess entropy, $-S_2(t)$, measured from sample A with three different Γ_{max} . *Inset* shows same data measured from samples B and C. The three datasets were fit by using Eq. 5 with $c = 3.9 \pm 0.2$ (solid line), 1.0 ± 0.1 (inset dash-dot line), and 1.4 ± 0.1 (inset dashed line) for samples A, B, and C, respectively.

collapsed data from sample A are well fit by Rosenfeld's equilibrium excess entropy scaling law,

$$\tau_{\alpha}(t - t_d) \sim e^{-cS_2(t)/k_B}, \quad [5]$$

where $c = 3.9 \pm 0.2$ is a constant prefactor (12).

Previous studies of the excess entropy scaling connect sample dynamics to static structure; in other words, a measurement of static structure and the scaling law can be used to predict sample dynamics. Our finding, although similar in form, has a somewhat different implication: The static structure is a consequence, rather than the cause, of the relaxation process. Slower particle rearrangement processes (τ_{α}) produce more ordered particle arrangements (S_2) that require longer waiting times (t_d) to observe. Furthermore, since the time delay, t_d , is explicitly encoded in Eq. 5, we can use information about the “current” sample static structure to learn about plastic flow and relaxation processes that occurred in the sample at earlier times. The structures “remember” sample dynamical history (50). In the future, application of this concept could provide insight about manufacturing and processing of amorphous materials wherein microstructures are altered by thermomechanical processing (5, 6). Note also, the “asynchronous” dynamics–structure connection observed in our oscillatory experiments is fully compatible with steady-state experiments. When $\dot{\Gamma}$ approaches a constant value, both $\tau_{\alpha}(t)$ and $t_d(t)$ lose their dependence on t , and the scaling framework evolves into a previous relationship found for glass-formers in uniform shear flows (16). Thus, we expect to see this transition from a non-steady-state to a quasi-steady-state by gradually increasing the oscillatory period in future studies.

To further examine the influence of material structure and other properties on the excess entropy scaling, we plot $\tau_{\alpha}(t - t_d)$ versus $S_2(t)$ for samples B and C (Fig. 4, *Inset*). Sample B is a monodisperse colloidal solid (Table 1) and thus has larger ordered domains (*SI Appendix*) compared to those in sample A. In this case, the combination of initial sample packing condition and shear-induced restructuring gives rise to much larger $|S_2|$ values, well above $4.5k_B$, a value that corresponds to the liquid-to-crystal transition observed in 2D colloidal samples (51). By comparison, sample C is a bidisperse mixture of much smaller particles (Table 1) and thus has stronger thermal particle motion; its $|S_2|$ values are between those of sample A and B. The short-time $F_s(\tau)$ for sample C is very close, but never equal to unity, unlike those measured in samples A and B (*SI Appendix*). We believe that this difference is caused by thermal motion at short times in sample C. Despite these differences in material properties, in all three samples, both τ_{α} and $|S_2|$ decrease with increasing shear rate (as in sample A). All experimental data thus demonstrate that excess entropy scaling with relaxation time exists independent of shear rate. The best fits to Eq. 5 yield $c = 1.0 \pm 0.1$ and 1.4 ± 0.1 , for samples B and C, respectively. In previous experiments with colloidal samples, the range of the dynamics is typically one decade by using multiple packing fractions. Our experiment achieves a similar dynamic range by changing shear rate alone. The excess entropy scaling form has been found to depend on factors including interfacial boundary conditions and the functional shape of the sample's pair potentials (16, 19, 29). For our amorphous samples with small crystalline domains separated by regions of disorder, to fully understand the difference in the prefactor c will require further investigation.

Finally, we also examined use of S_2^{θ} computed from directional $g(r, \theta)$; here, θ is the direction relative to shear. Unfortunately, the noise in $g(r, \theta)$ at long distances prevents Eq. 4 from converging within the finite cutoff distance (*SI Appendix*). In steady-state measurements, this sampling noise can be suppressed by time averaging. In non-steady-state samples, however, time averaging

necessarily involves integration over a broader range of shear rates, which complicates evaluation of sample static structure. In the future, this issue could be ameliorated by using a much larger sample size. Our observation that τ_{α} scales with S_2 indicates a major difference in the microscopic relaxation mechanism between amorphous solids with small ordered domains separated by regions of disorder and the more disordered glassy samples. In the latter, τ_{α} has been found to scale better with the extensional excess entropy, S_2^{θ} , which is derived from $g(r, \theta = \pi/4)$ (14, 16). The deformation along the extensional direction ($\theta = \pi/4$) has been argued to create more accessible configurations (that is, smaller $|S_2|$ values) that facilitate faster relaxation rates (16). In sheared amorphous samples with small crystalline domains separated by regions of disorder, by contrast, particle rearrangements likely occur through cooperative sliding motions along grain boundaries, whose orientations depend on the sample's initial condition and become randomized when sample size is much larger than grain size. Therefore, we expect particle rearrangements to be less sensitive to shear in our polycrystal-like solids (35, 36, 44).

In summary, we have developed a framework to understand plastic-flow-induced dynamics in deformed amorphous colloids with different degrees of polycrystallinity. The framework extends the concept of excess entropy scaling from equilibrium to nonequilibrium nonstationary states. Our experiment demonstrates excess entropy scaling in nonequilibrium materials. Experimental data comprising a wide range of shear rates, relaxation times, particle pair correlations, and excess entropy reveal that transient shear-induced relaxation times scale as a simple exponential function of excess entropy. Collectively, these results demonstrate, in nonstationary states, that increasing (decreasing) strain rates leads to faster (slower) relaxation, which, in turn, results in more disordered (ordered) microstructures. The work also reveals a power-law connection between bulk shear rate and bulk viscous relaxation time that characterizes sample shear-thinning behavior; using the observation of excess entropy scaling, we thus deduce that shear thinning is controlled by microscopic structure. Notably, we find that new parameters, specifically lag times between shear rates, relaxation times, and excess entropy, are crucial for proper application of the excess entropy concept in nonstationary conditions. In the future, it should be interesting to compare microscopic relaxation channels and shear-induced structural anisotropy in polycrystals versus more traditional glasses. Also, in addition to uniform and oscillatory shear, it would be desirable to test excess entropy scaling in more general strain protocols in both 2D and three-dimensional systems.

Materials and Methods

Interfacial Stress Rheometer. The experiments used a custom-made interfacial stress rheometer (32, 33). Briefly, a pair of vertical glass walls pinned a water/decane interface, as shown in Fig. 1A. A magnetic needle was located between and was parallel to the glass walls; it was held by capillary forces at the interface. Water height was adjusted so that the interface was flat between the two walls and needle. A pair of Helmholtz coils imposed a sinusoidal magnetic force on the needle that translated it axially. The out-of-plane Lorentz forces (approximately 10^{-16} N) were negligibly small compared with interfacial trapping forces (approximately 10^{-2} N). The moving needle and the two fixed boundaries thus created a flat, 2D shearing channel. A microscope (Infinity, K2) and high-resolution camera (IO Industries, Flare 4M180) were employed to measure the motions of the needle and interface-bound colloidal particles (31, 33).

Sample Preparation. The colloidal suspensions were composed of sulfate latex particles (Invitrogen) with different diameters. The particles were injected onto the interface by using a pipette, and regions of approximately 80×200 particles were studied. Due to the small particle sizes ($< 10 \mu\text{m}$), capillary interactions were small and unimportant (52, 53). A long-range dipole-dipole repulsion between particles (54) caused the spheres to

assemble into a disordered, jammed, 2D structure with large amorphous areas filling the regions between randomly oriented microcrystal domains (Fig. 1 B and C and *SI Appendix*). Characteristics of the three investigated particle systems such as particle type, packing fraction, mean interparticle separation, d (derived from particle pair correlation functions), and strain amplitude are summarized in Table 1. The camera recorded the needle displacement and all particle motions; trajectories were extracted from the images by using standard particle-tracking software (55). The experiments thus measured the particle positions, strain rate, relaxation time, and excess entropy versus time during the shear cycle. We sheared the samples at a fixed low frequency of 0.1 Hz to reduce/remove hydrodynamic effects. Additionally, we have calculated the Boussinesq number, $Bq = |\eta^*|/D\eta$, wherein η^* is the complex interfacial viscosity, D the needle diameter, and η the mean viscosity of the oil and water (56, 57). Bq quantifies the ratio between the in-plane and out-of-plane stresses induced by the needle. We find that $Bq = 147.5$ and 101.5 for samples A and B, respectively, corroborating the expectation that hydrodynamic flows in the water and oil phases are negligible. The relaxation processes are due to plastic events that occur when the samples are stressed beyond yield.

Affine and Nonaffine Particle Motions. To compute the y -dependent mean particle displacement, $\Delta x(y)$, along the shear (x) direction, we first computed $[y_j(t), \Delta x_j(t)]$ from all particles at time t ; $\Delta x(y)$ was then obtained from the fit of $[y_j(t), \Delta x_j(t)]$ (*SI Appendix*). The local strain is thus $\gamma(y, t) = \partial \Delta x(y, t) / \partial y$. To account for the slightly nonlinear flow profile (*SI Appendix, Fig. S1*), $\Delta x(y, t)$ and $\gamma(y, t)$ were fit by a polynomial of y up to the third and second orders, respectively. To characterize the overall affine deformation, we defined $\Gamma(t)$ as the spatial average (over y) of $\gamma(y, t)$. The nonaffine particle displacement, $\Delta \bar{r}_j^2 \equiv \{\Delta x_j^2, \Delta y_j^2\}$ between times t and $t + \tau$, was obtained by subtracting the affine contribution from the total horizontal displacement, $\Delta x_j^2(\tau) = x_j(t + \tau) - x_j(t) - \Delta x(y_j, \tau)$. Since the net flow in y direction is zero, $\Delta y_j^2(\tau) = y_j(t + \tau) - y_j(t)$.

Calculation of $\langle |\dot{\Gamma}| \rangle_{\delta t}$. To determine $\langle |\dot{\Gamma}| \rangle_{\delta t}$, we defined a triangle kernel function centered at t , $\Lambda(t, s) \equiv \max(\delta t/2 - |s - t|, 0)$, and we computed the convolution: $\langle |\dot{\Gamma}| \rangle_{\delta t} = \langle |\dot{\Gamma}| * \Lambda \rangle(t) \equiv \int_{-\infty}^{\infty} |\dot{\Gamma}(t - t')| \Lambda(t') dt'$. (Note, Λ was normalized before the convolution.) This parameter-free approach places maximal weight on the shear rate at t and zero weight on those shear rates outside of $[t - \delta t/2, t + \delta t/2]$. We also tested convolution with a Gaussian kernel function, and the results were very similar (*SI Appendix*).

Evaluation of Δt and t_d . To determine Δt , we computed the (unnormalized) correlation function, $C_1(\Delta t) \equiv \langle (|\dot{\Gamma}(t)|)_{\delta t} - \langle (|\dot{\Gamma}(t)|)_{\delta t} \rangle \tau_{\alpha}^{-1}(t + \Delta t) - \langle \tau_{\alpha}^{-1}(t + \Delta t) \rangle \rangle$; here, Δt is the trial lag time, and $\langle \dots \rangle$ represents time average. The value of Δt wherein $C_1(\Delta t)$ reaches its maximal value was set to be the true lag time between $\langle (|\dot{\Gamma}(t)|)_{\delta t} \rangle$ and $\tau_{\alpha}^{-1}(t)$ (*SI Appendix*). To determine t_d , we similarly computed the (unnormalized) correlation function, $C_2(h) \equiv \langle |S_2(t)| \tau_{\alpha}(t - h\tau_{\alpha}) \rangle$ as a function of h . Similar to the procedure above, $C_2(h)$ is maximized when $h\tau_{\alpha}$ (or equivalently, t_d) is closest to the true time lag between $|S_2(t)|$ and $\tau_{\alpha}(t)$ (*SI Appendix*).

Data Availability. All data discussed in the paper are available in the main text and *SI Appendix*.

ACKNOWLEDGMENTS. We thank Kevin Aptowicz, Piotr Habdas, Peter Collings, Remi Dreyfus, Chandan Kumar Mishra, Alexis de la Cotte, Analisa Hill, Sophie Ettinger, Wei-shao Wei, Andrea Liu, Doug Durian, Sébastien Kosgodagan Acharige, and Xiaozhou He for helpful discussions. This work was primarily supported by the NSF through Penn Materials Research Science and Engineering Center Grant DMR-1720530, including its Optical Microscopy Shared Experimental Facility. Additionally, X.M. and A.G.Y. were supported by NSF Grant DMR16-07378 and NASA Grant 80NSSC19K0348. K.L.G., D.J.J., and P.E.A. were supported by Army Research Office Grant W911-NF-16-1-0290.

- N. J. Balmforth, I. A. Frigaard, G. Ovarlez, Yielding to stress: Recent developments in viscoplastic fluid mechanics. *Annu. Rev. Fluid Mech.* **46**, 121–146 (2014).
- D. Bonn, M. M. Denn, L. Berthier, T. Divoux, S. Manneville, Yield stress materials in soft condensed matter. *Rev. Mod. Phys.* **89**, 035005 (2017).
- A. Nicolas, E. E. Ferrero, K. Martens, J.-L. Barrat, Deformation and flow of amorphous solids: Insights from elastoplastic models. *Rev. Mod. Phys.* **90**, 045006 (2018).
- J. R. Seth, L. Mohan, C. Locatelli-Champagne, M. Cloitre, R. T. Bonnecaze, A micromechanical model to predict the flow of soft particle glasses. *Nat. Mater.* **10**, 838–843 (2011).
- O. Engler, J. Hirsch, Texture control by thermomechanical processing of AA6xxx Al-Mg-Si sheet alloys for automotive applications—A review. *Mater. Sci. Eng. A* **336**, 249–262 (2002).
- Y. Sun, A. Concustell, A. Lindsay Greer, Thermomechanical processing of metallic glasses: Extending the range of the glassy state. *Nat. Rev. Mater.* **1**, 16039 (2016).
- M. L. Falk, J. S. Langer, Dynamics of viscoplastic deformation in amorphous solids. *Phys. Rev. E* **57**, 7192–7205 (1998).
- P. Schall, D. A. Weitz, F. Spaepen, Structural rearrangements that govern flow in colloidal glasses. *Science* **318**, 1895–1899 (2007).
- W. Götze, *Complex Dynamics of Glass-Forming Liquids: A Mode-Coupling Theory* (Oxford University Press, New York, NY, 2008).
- T. R. Kirkpatrick, D. Thirumalai, P. G. Wolynes, Scaling concepts for the dynamics of viscous liquids near an ideal glassy state. *Phys. Rev. A Gen. Phys.* **40**, 1045–1054 (1989).
- V. Lubchenko, Shear thinning in deeply supercooled melts. *Proc. Natl. Acad. Sci. U.S.A.* **106**, 11506–11510 (2009).
- Y. Rosenfeld, Relation between the transport coefficients and the internal entropy of simple systems. *Phys. Rev. A* **15**, 2545–2549 (1977).
- M. Dzugutov, A universal scaling law for atomic diffusion in condensed matter. *Nature* **381**, 137–139 (1996).
- W. P. Krekelberg, V. Ganesan, T. M. Truskett, Shear-rate-dependent structural order and viscosity of a fluid with short-range attractions. *Phys. Rev. E* **78**, 010201 (2008).
- E. H. Abramson, Viscosity of carbon dioxide measured to a pressure of 8 GPa and temperature of 673 K. *Phys. Rev. E* **80**, 021201 (2009).
- T. S. Ingebrigtsen, H. Tanaka, Structural predictor for nonlinear sheared dynamics in simple glass-forming liquids. *Proc. Natl. Acad. Sci. U.S.A.* **115**, 87–92 (2018).
- J. C. Dyre, Perspective: Excess-entropy scaling. *J. Chem. Phys.* **149**, 210901 (2018).
- A. Baranyai, D. J. Evans, Direct entropy calculation from computer simulation of liquids. *Phys. Rev. A* **40**, 3817–3822 (1989).
- X. G. Ma et al., Test of the universal scaling law of diffusion in colloidal monolayers. *Phys. Rev. Lett.* **110**, 078302 (Feb 2013).
- A. Samanta, S. M. Ali, S. K. Ghosh, New universal scaling laws of diffusion and Kolmogorov-Sinai entropy in simple liquids. *Phys. Rev. Lett.* **92**, 145901 (2004).
- J. J. Hoyt, M. Asta, B. Sadigh, Test of the universal scaling law for the diffusion coefficient in liquid metals. *Phys. Rev. Lett.* **85**, 594–597 (2000).
- A. Samanta, S. M. Ali, S. K. Ghosh, Universal scaling laws of diffusion in a binary fluid mixture. *Phys. Rev. Lett.* **87**, 245901 (2001).
- J. Mittal, J. R. Errington, T. M. Truskett, Thermodynamics predicts how confinement modifies the dynamics of the equilibrium hard-sphere fluid. *Phys. Rev. Lett.* **96**, 177804 (2006).
- W. P. Krekelberg et al., Generalized Rosenfeld scalings for tracer diffusivities in not-so-simple fluids: Mixtures and soft particles. *Phys. Rev. E* **80**, 061205 (2009).
- W. P. Krekelberg, V. Ganesan, T. M. Truskett, Structural signatures of mobility on intermediate time scales in a supercooled fluid. *J. Chem. Phys.* **132**, 184503 (2010).
- M. J. Pond, J. R. Errington, T. M. Truskett, Communication: Generalizing Rosenfeld's excess-entropy scaling to predict long-time diffusivity in dense fluids of Brownian particles: From hard to ultrasoft interactions. *J. Chem. Phys.* **134**, 081101 (2011).
- C.-H. Wang, S.-H. Yu, P. Chen, Universal scaling laws of diffusion in two-dimensional granular liquids. *Phys. Rev. E* **91**, 060201 (2015).
- L. Ning et al., Universal scaling law for colloidal diffusion in complex media. *Phys. Rev. Lett.* **122**, 178002 (2019).
- X. Ma, J. Liu, Y. Zhang, P. Habdas, A. G. Yodh, Excess entropy and long-time diffusion in colloidal fluids with short-range interparticle attraction. *J. Chem. Phys.* **150**, 144907 (2019).
- B. Li et al., Breakdown of diffusivity-entropy scaling in colloidal glass-forming liquids. *Commun. Phys.* **1**, 79 (2018).
- G. T. Shahin, "The stress deformation interfacial rheometer," PhD thesis, University of Pennsylvania, Philadelphia, PA (1986).
- P. Moldenaers, J. Vermant, S. Reynaert, C. F. Brooks, G. G. Fuller, Analysis of the magnetic rod interfacial stress rheometer. *J. Rheol.* **52**, 261–285 (2008).
- N. C. Keim, P. E. Arratia, Yielding and microstructure in a 2D jammed material under shear deformation. *Soft Matter* **9**, 6222–6225 (2013).
- N. C. Keim, P. E. Arratia, Mechanical and microscopic properties of the reversible plastic regime in a 2D jammed material. *Phys. Rev. Lett.* **112**, 028302 (2014).
- T. Hamanaka, H. Shiba, A. Onuki, Plastic flow in polycrystal states in a binary mixture. *Phys. Rev. E* **77**, 042501 (2008).
- H. Shiba, A. Onuki, Plastic deformations in crystal, polycrystal, and glass in binary mixtures under shear: Collective yielding. *Phys. Rev. E* **81**, 051501 (2010).
- R. Yamamoto, A. Onuki, Dynamics of highly supercooled liquids: Heterogeneity, rheology, and diffusion. *Phys. Rev. E* **58**, 3515–3529 (1998).
- L. Cipolletti, S. Manley, R. C. Ball, D. A. Weitz, Universal aging features in the restructuring of fractal colloidal gels. *Phys. Rev. Lett.* **84**, 2275–2278 (2000).
- D. El Masri, M. Pierno, L. Berthier, L. Cipolletti, Ageing and ultra-slow equilibration in concentrated colloidal hard spheres. *J. Phys. Condens. Matter* **17**, S3543–S3549 (2005).
- A. Madsen, R. L. Leheny, H. Guo, M. Sprung, O. Czakkel, Beyond simple exponential correlation functions and equilibrium dynamics in x-ray photon correlation spectroscopy. *New J. Phys.* **12**, 055001 (2010).

41. S. Mazoyer, L. Cipolletti, L. Ramos, Direct-space investigation of the ultraslow ballistic dynamics of a soft glass. *Phys. Rev. E* **79**, 011501 (2009).
42. R. Angelini *et al.*, Glass–glass transition during aging of a colloidal clay. *Nat. Commun.* **5**, 4049 (2014).
43. N. Gnan, E. Zaccarelli, The microscopic role of deformation in the dynamics of soft colloids. *Nat. Phys.* **15**, 683–688 (2019).
44. E. Tamborini, L. Cipolletti, L. Ramos, Plasticity of a colloidal polycrystal under cyclic shear. *Phys. Rev. Lett.* **113**, 078301 (2014).
45. J. H. Simmons, R. K. Mohr, C. J. Montrose, Non-Newtonian viscous flow in glass. *J. Appl. Phys.* **53**, 4075–4080 (1982).
46. L. Berthier, J.-L. Barrat, J. Kurchan, A two-time-scale, two-temperature scenario for nonlinear rheology. *Phys. Rev. E* **61**, 5464–5472 (2000).
47. X. Cheng, J. H. McCoy, J. N. Israelachvili, I. Cohen, Imaging the microscopic structure of shear thinning and thickening colloidal suspensions. *Science* **333**, 1276–1279 (2011).
48. R. G. Larson, *The Structure and Rheology of Complex Fluids* (Oxford University Press, New York, NY, 1999).
49. H. Tanaka, T. Kawasaki, H. Shintani, K. Watanabe, Critical-like behaviour of glass-forming liquids. *Nat. Mater.* **9**, 324–331 (2010).
50. N. C. Keim, J. D. Paulsen, Z. Zeravcic, S. Sastry, S. R. Nagel, Memory formation in matter. *Rev. Mod. Phys.* **91**, 035002 (2019).
51. Z. Wang, A. M. Alsayed, A. G. Yodh, Y. Han, Two-dimensional freezing criteria for crystallizing colloidal monolayers. *J. Chem. Phys.* **132**, 154501 (2010).
52. P. Pieranski, Two-dimensional interfacial colloidal crystals. *Phys. Rev. Lett.* **45**, 569–572 (1980).
53. P. A. Kralchevsky, K. Nagayama, Capillary interactions between particles bound to interfaces, liquid films and biomembranes. *Adv. Colloid Interface Sci.* **85**, 145–192 (2000).
54. J. Vermant, B. J. Park, E. M. Furst, Heterogeneity of the electrostatic repulsion between colloids at the oil–water interface. *Soft Matter* **6**, 5327–5333 (2010).
55. D. Allan *et al.*, soft-matter/trackpy: Trackpy, Version 0.4.2. <https://doi.org/10.5281/zenodo.3492186>. Accessed 16 October 2019.
56. C. F. Brooks, G. G. Fuller, C. W. Frank, C. R. Robertson, An interfacial stress rheometer to study rheological transitions in monolayers at the air–water interface. *Langmuir* **15**, 2450–2459 (1999).
57. T. Verwijlen, P. Moldenaers, H. A. Stone, J. Vermant, Study of the flow field in the magnetic rod interfacial stress rheometer. *Langmuir* **27**, 9345–9358 (2011).